Earthquake Research Advances 1 (2021) 100001

Contents lists available at ScienceDirect

Earthquake Research Advances

journal homepage: www.keaipublishing.com/en/journals/earthquake-research-advances

Illuminating high-resolution crustal fault zones using multi-scale dense arrays and airgun source

Hongfeng Yang [a,b,*], Yaohui Duan [a], Junhao Song [a], Weitao Wang [c], Wei Yang [c], Xiaofeng Tian [d], Baoshan Wang [e]

[a] Earth System Science Programme, Faculty of Science, The Chinese University of Hong Kong, Hong Kong, China
[b] Shenzhen Research Institute, The Chinese University of Hong Kong, Shenzhen, China
[c] Institute of Geophysics, China Earthquake Administration, Beijing, China
[d] Center of Geophysical Exploration, China Earthquake Administration, Zhengzhou, China
[e] School of Earth and Space Sciences, University of Science and Technology of China, Hefei, China

ARTICLE INFO

Keywords:
Fault zone
Temporal changes
Dense array
Airgun source

ABSTRACT

High-resolution imaging of fault zone structure and its temporal changes can not only advance our understanding of earthquake physics, but is also critical for better seismic hazard preparation and mitigation. In the past a few years, we deployed multi-scale dense arrays across the Chenghai fault system in Binchuan, Yunnan, China. The first array consisted of 381 intermediate-period three-component seismometers with an average station spacing of ~2 km. The array has been deployed in the field for ~3 months in 2017 and recorded numerous local and teleseismic earthquakes. Travel time analyses based on teleseismic earthquakes and an airgun source in the region indicated clear signature of low-velocity fault zones in the southern branch of the Chenghai fault system. In 2018 we deployed two other linear arrays using the same instruments with much smaller inter-station spacing, e.g. 30–50 m, across the southern branch the Chenghai fault. The profile lengths were 8 and 5 km, respectively. Record sections of the airgun source on the two linear arrays clearly marked a low-velocity zone (LVZ) within the southern array but no such signature in the northern array, suggesting along-strike variation of the LVZ. Although the instruments within our dense arrays had an intermediate frequency band, we demonstrated that they were capable of characterizing crustal structure with techniques commonly applied to broadband signals such as receiver functions. To our best knowledge, this was the first time to have multi-scale across-fault dense arrays with three-component seismometers in such apertures. These results lay out the pavement to comprehensively investigate fault zone structures as well as to derive subsurface structural changes using dense arrays and the airgun source.

1. Introduction

Earthquakes occur on faults and thus earthquake generation and rupture propagation are controlled by fault zone properties including stress distribution (Duan and Oglesby, 2006; Ripperger et al., 2007; Yang et al., 2012, 2019a, 2019b; Weng et al., 2015, 2019b), fault geometry, step overs, and branches (Bhat et al., 2007; Yang et al., 2013; Ryan and Oglesby, 2014; Yu et al., 2018), as well as frictional and material properties (Harris and Day, 1997; Huang and Ampuero, 2011; Weng et al., 2016; Weng and Yang, 2018; Yao and Yang, 2020; Chen et al., 2021). Geological studies of exhumed faults and results from active fault drilling into seismogenic depths indicate that most tectonic deformation is accommodated in the fault core (*e.g.* Chester and Logan, 1986; Chester et al., 1993; Sieh et al., 1993; Johnson et al., 1994; Ma et al., 2006; Ujiie et al., 2013). Surrounding the fault core is a zone composed of highly fractured materials, termed fault zone (FZ) (*e.g.* Chester and Logan, 1986;

* Corresponding author. Earth System Science Programme, Faculty of Science, The Chinese University of Hong Kong, Hong Kong, China.
E-mail address: hyang@cuhk.edu.hk (H. Yang).

Production and Hosting by Elsevier on behalf of KeAi

https://doi.org/10.1016/j.eqrea.2021.100001
Received 6 May 2020; Received in revised form 5 October 2020; Accepted 13 October 2020
2772-4670/© 2021 China Earthquake Networks Center. Publishing services by Elsevier B.V. on behalf of KeAi Communications Co. Ltd. This is an open access article under the CC BY license (http://creativecommons.org/licenses/by/4.0/).

Schulz and Evans, 1998, 2000), where seismic velocities are significantly reduced relative to the host rocks. Such low-velocity zone (LVZ) is often interpreted as a result of accumulative damages from past earthquakes, hence the term 'fault damage zones'. It has been suggested that the LVZ structure and its temporal variation hold critical keys for a better understanding of earthquake physics, evolution of fault systems and hazard mitigation (e.g. Kanamori, 1994; Li et al., 1998; Vidale and Li, 2003; Yang, 2015). Furthermore, material properties of the LVZ may also influence the migration of hydrocarbons and fluids, as well as surface geomorphology (e.g. Wibberley et al., 2008; Faulkner et al., 2010). High-resolution imaging of the FZ structure and its temporal changes is thus highly demanded.

The damage zone, or the LVZ, often has a width of hundreds of meters to several kilometers and a 20–60% reduction in P- and S-wave velocities (e.g. Ben-Zion and Sammis, 2003; Yang, 2015). Numerous investigations based on dynamic rupture simulations have suggested that the LVZ exerts significant influence on properties of earthquake ruptures (*e.g.* Harris and Day, 1997; Huang and Ampuero, 2011; Huang et al., 2014; Weng et al., 2016; Chen and Yang, 2020). For instance, Weng et al. (2016) have found that the LVZ can promote rupture extents and thus increase earthquake sizes. Such promotional effects hold true even for a LVZ extending to shallow depths (Weng et al., 2016). In addition, the LVZ may amplify ground motion near faults (*e.g.* Wu et al., 2009; Avallone et al., 2014; Song and Yang, 2021) and may influence long-term deformation processes in the crust (*e.g.* Finzi et al., 2009; Kaneko et al., 2011). The amplified near-field ground velocities may lead to considerable uncertainties in estimating frictional parameters such as the critical slip weakening distance on seismogenic faults (Chen and Yang, 2020). Moreover, cracks in the LVZ may cause stress rotation (Faulkner et al., 2006) and control movement of fluids, which in turn play an important role in affecting the fault strength (Eberhart-Phillips et al., 1995; Yehya et al., 2018). These findings significantly highlight the importance of investigating the LVZ structure and its effects on earthquake generation and rupture propagation.

Furthermore, seismic velocities in the LVZ may be changed over time around a large earthquake due to opening/closure of cracks or fault zone dilation/compaction, which has been interpreted as fault zone damage and healing processes (Li et al., 1998; Vidale and Li, 2003; Schaff and Beroza, 2004; Rubinstein and Beroza, 2004; Peng and Ben-Zion, 2006; Brenguier et al., 2008; Zhao and Peng, 2009). For instance, changes in travel times of identical source-receiver pairs across the Jonson Valley fault indicated 1% increase in both v_P and v_S from 1994 to 1996, a few years after the 1992 M_W7.3 Landers earthquake (Li et al., 1998). To accurately document temporal variation of the LVZ structure in the field requires high-quality repeating sources, such as repeating earthquakes (e.g., Schaff and Beroza, 2004; Rubinstein and Beroza, 2004; Peng and Ben-Zion, 2006; Zhao and Peng, 2009) or man-made seismic sources (e.g. Li et al., 1998; Vidale and Li, 2003). Repeating earthquakes are spatially limited and may suffer from eliminating the effects of imperfect identical source locations. Man-made seismic sources such as explosions are usually used in the investigation of structural variation over time. Although the explosives are buried within a small distance (e.g. 10 m) with previous ones, they are imperfect repeatable sources and may lead to considerable uncertainties in estimating the relatively small changes in velocity over time. Moreover, explosion-type sources can only be detonated sporadically, which prevents continuous monitoring of the temporal changes in subsurface structure.

More recently, a new artificial seismic source has been implemented in probing high-resolution temporal changes of crustal velocities, termed Fixed Airgun Signal Transmitting Station (FASTS) (Chen et al., 2017). The core part of the FASTS is an airgun array that can suddenly release large-volume compressed air and repeat in a short time. In April 2011, the first FASTS was started to build in the Dayindian reservoir at Binchuan, Yunnan, southwest China (Fig. 1). During the year of 2013, thousands of airgun shots have been conducted in Binchuan, Yunnan, with an average number of 30 per day. Signals of the airgun shots were found nearly identical with cross-correlation coefficients larger than 0.99 (Wang et al., 2012; Chen et al., 2017), providing an unprecedented opportunity to continuously monitor the temporal variation of subsurface structure. For example, Wang et al. (2020) used a one-week dataset excited by the Binchuan FASTS to derive diurnal and semidiurnal velocity changes underground. The amplitudes of velocity changes are as small as 10^{-4} – 10^{-3}. By utilizing a downhole airgun source, Yang et al. (2018) reported subsurface velocity changes within one week near the Xiaojiang fault zone in Yunnan, China, which agreed well with the variation in groundwater level.

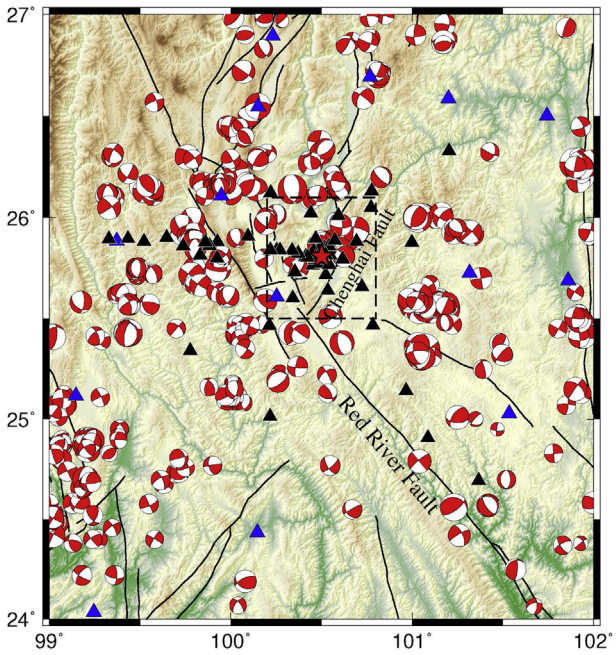

Fig. 1. Locations of the Fixed Airgun Signal Transmitting Station (FASTS) (red star) and seismic stations (Black triangles: FASTS network; blue triangles: Yunnan seismic network). Faults are shown in black lines. Beach balls denote focal mechanism solutions for earthquakes in the region from 2000 to 2014 (Xu et al., 2020).

To delineate fault zone structures and track temporal changes by utilizing the FASTS, we have deployed multi-scale dense arrays in the Binchuan basin, Yunnan in the past a few years. In this work we show the unique data recordings and signatures of teleseismic travel times, as well as waveforms from the airgun source. We then highlight the opportunity to continuously illuminate crustal fault zones with high resolution using dense arrays and high-quality airgun sources. We also discuss the possibility to derive crustal structure from such small-aperture dense array and challenges to infer the preparation process of earthquakes.

2. Tectonic setting and permanent seismic network

The study region is surrounded by the northern portion of the NW-SE trending Red River Fault (RRF) and the nearly N–S trending Chenghai Fault (CHF), a seismically active region with frequent large earthquakes (Wang et al., 2015). In the past 500 years, four earthquakes with magnitudes greater than 7.0 have occurred in this region, and the most recent one was the 1996 *M*7.0 Lijiang earthquake (Zhou et al., 2004). The northern portion of the RRF and neighboring faults accommodate regional E-W crustal extension and N–S shortening due to the Indo-Eurasia collision (Allen et al., 1984), and has consequently experienced strong earthquakes including the 1925 *M*7.0 Dali earthquake (Zhou et al., 2004). Moment tensor solutions of earthquakes from 2000 to 2014 exhibited complex faulting mechanisms (Fig.1). Although most earthquakes showed strike-slip focal mechanisms, normal and thrust earthquakes distributed throughout the region (Xu

et al., 2020), with depths concentrating in the upper crust (Yang and Yao, 2021).

The CHF extends ~200 km from Yongsheng in the north and intersects with the RRF in the south (Fig. 1). Measurements of across-fault leveling and baseline were used to obtain a recent estimate of ~4–10 mm/yr slip rates on the CHF (Zhang and Liu, 2016). The largest earthquake occurred on the CHF in 1515 near Yongsheng and the magnitude was inferred as M7$^3/_4$ (Zhou et al., 2004; Wang et al., 2015). Recurrence interval of M7 earthquakes on the CHF was suggested to be more than 1500 years according to paleo-seismological records (Yu et al., 2005). Additionally, the most recent magnitude 6.0 earthquake occurred in the north portion of the CHF near Yongsheng in 2001.

After the FASTS was constructed in Binchuan, 40 intermediate-period seismic stations have been deployed to complement the present Yunnan permanent seismic network (Fig. 1). These stations have a sample rate of 100 points per second. One station has been deployed less than 50 m from the airgun source to record waveforms that approximate the source time function. Since 2012, numerous earthquakes within 100 km of the FASTS have been recorded, among which the largest one is the 2013 M_W5.5 Eryuan earthquake. One profile with 15 stations has been deployed between the FASTS and the 2013 earthquake to monitor subsurface structure and temporal variation. Overall the seismic network is well in place to continuously monitor temporal changes of crustal structure in a local distance (Fig. 1).

Seasonal and daily variations of subsurface structure have been derived at these stations using the FASTS in Binchuan (Luan et al., 2016, 2017; Liu et al., 2021). After carefully inspecting and eliminating the effect of reservoir water level on waveform recordings, Luan et al. (2016) suggested that four stations in the Binchuan basin have shown signature of subsurface seasonal variation based on the data in 2013 (Fig. 2b). Furthermore, daily variation of the shallow subsurface structure was identified by utilizing one-month recording with 24 airgun shots per day in 2015 (Luan et al., 2017). However, the water level changes in the reservoir were suggested to change the dominant frequency of the airgun signals (Luan et al., 2016), which may in turn affect the measurement of travel time variation. As shown in the results using the yearly data in 2016, Liu et al. (2021) observed that the seasonal changes of travel time were inversely correlated with the frequency variation, which was caused by the water level fluctuation. Furthermore, when comparing the travel time changes derived from the airgun data with those from ambient noise cross correlation, Liu et al. (2021) found the amplitudes of seasonal changes in travel time from the two methods differed significantly, with the one from airgun being at least one order of magnitude larger than those from noise. Therefore, how to derive robust and reliable seasonal variation from the airgun data remains unclear, due to the significant variation in water level of the reservoir in Binchuan.

3. Temporary arrays

Although the existing network provides the basic coverage to monitor local seismicity and subsurface velocity variation (Luan et al., 2016, 2017), it is insufficient to be used for the high-resolution imaging and temporal variation tracking in the fault zone. Furthermore, the recorded waveforms of the airgun source are more complex than a simple explosion source. Due to the irregular geometry of the reservoir, the waveform recorded at the nearest station may not be a good approximation of the airgun source time function. Therefore, a dense array has been deployed in Binchuan from March to May in 2017 to capture the characteristics of full wavefield of the airgun signals (Xu et al., 2018).

The Array of Binchuan (ABC) spans approximately 50 km by 50 km in Binchuan basin and covers the southern portion of the CHF (Fig. 2a). It is composed of 381 intermediate-period seismometers (QS-05A 5 s), which is an all-in-one unit with a Li-Ion battery that can last up to two months. The average spacing of the array is ~2 km (Fig. 2a). It has been operating in the field for two months, during which 31 teleseismic earthquakes and 62 local earthquakes were recorded (Xu et al., 2018; Zhang et al., 2020). In addition, the FASTS excited airgun shots for ~10 times per day, providing an excellent dataset to image the LVZ structure of the CHF.

Based on preliminary analysis of P-wave travel times of teleseismic earthquakes and airgun shots (to be described in the next section), we identified segmented LVZ signature of the CHF. Therefore, we deployed another two linear dense arrays across two segments of the CHF with a much smaller spacing, ~40 m. In detail, one profile is 8 km in length and consists of 125 sensors, across the southern portion of the CHF where LVZ was identified from travel time anomalies recorded by the ABC array (Fig. 2b). The other one has 80 seismometers and is ~5 km in length (station spacing ~60 m) across the northern segment of the CHF, which is beyond the ABC array coverage (Fig. 2b).

4. Travel times of teleseismic earthquakes and airgun source

We first manually picked P-wave arrivals for teleseismic earthquakes recorded by the ABC array. For instance, the P-wave travel times from an M_W 6.8 teleseismic earthquake which occurred in the southern Pacific on

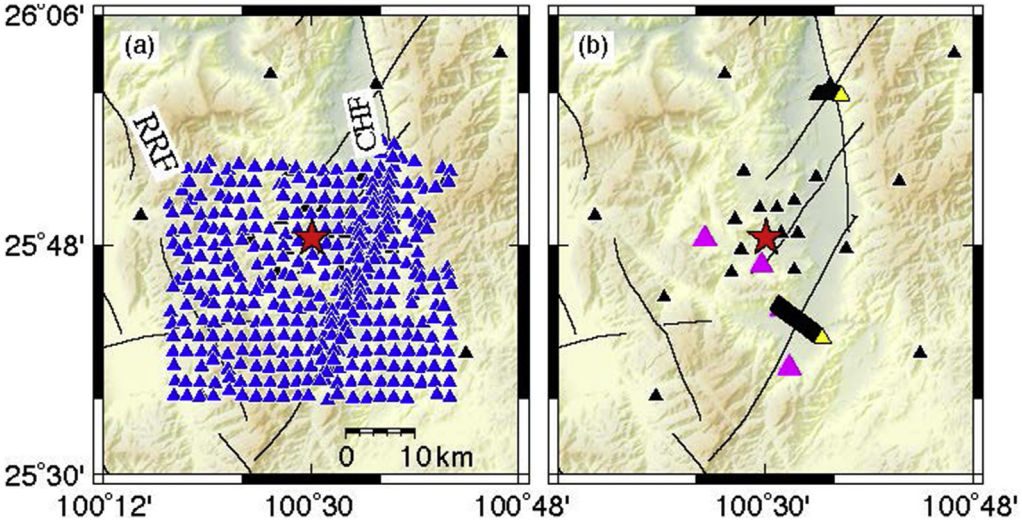

Fig. 2. Locations of the temporary arrays, permanent stations (black triangles), and the FASTS (red star) in the Binchuan basin, Yunnan. (a) blue triangles denote the ABC array (2017.03–05). RRF: Red River Fault; CHF: Chenghai Fault. (b) yellow triangles denote the newly deployed array (2018.01–02) across the CHF. Pink triangles show stations that were identified to have seasonal variations of subsurface structure using the FASTS data (Luan et al., 2016).

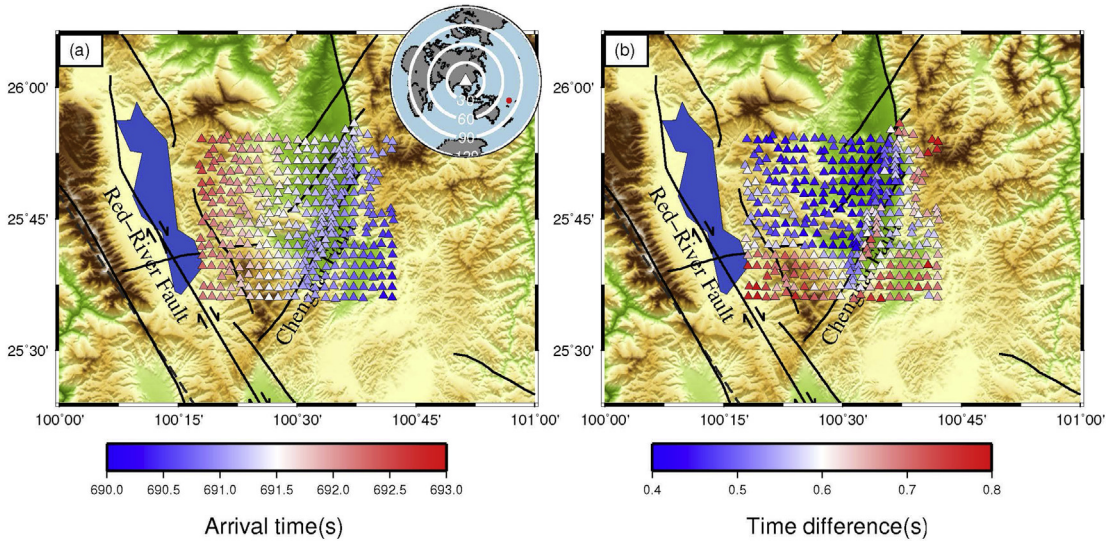

Fig. 3. P-wave arrivals for one teleseismic earthquake (a) and the differential times between observations and theoretical estimates from a 1-D velocity model (b). The top inset in (a) shows the location of event (red circle) used for the pick of arrivals. The triangle in the center of the figure indicates the location of the study region. The different color bars are displayed at the bottom.

May 9th, 2017 increase systematically with the corresponding distances as expected (Fig. 3a). We then calculated theoretical P-wave travel times using the 1-D IASP91 model and subtracted the theoretical travel times from observations, following the approach in Yang et al., (2020a). The differential times between theoretical estimates and observations illuminate clear signature of heterogeneous local structure. The differential times are all positive in the region (Fig. 3b), indicating that the local velocity is slower than the global average velocity predicted by the 1-D model. The relatively large travel time anomalies (slower regions) are mostly associated with the periphery of the array in the south and northeast, with one exception in the basin that is well associated with the CHF (Fig. 3b). Although the station spacing limits the resolution of estimating the LVZ structure of faults, the feature of the low velocity zone is still striking and intriguing.

We performed the same analysis for P-wave travel times of the FASTS signal. All travel times were fit with a linear trend with distance and the best fit yielded an apparent P-wave velocity of 5.13 km/s (Fig. 4a). Here we estimated the theoretical travel times from the apparent velocity and subtracted them from observations to obtain the differential times (Fig. 4b). The differential times are positive along the same portion of the CHF that shows anomalies in the teleseismic differential times (Fig. 3b), indicating the existence of LVZ. Another LVZ exists within the Binchuan basin, which is also revealed by the local earthquake tomography using the same data set (Zhang et al., 2020). Note that the differential time patterns are not identical for the FASTS and teleseismic earthquakes, mostly due to the different local ray paths from the FASTS source.

Travel time anomalies from both teleseismic and airgun events show that only a portion of the CHF exhibit clear LVZ characteristic, while the southernmost portion in the array coverage do not appear to have a LVZ. Such along-strike variation is similar to what have been found along the San Jacinto fault in southern California (Yang et al., 2014). Due to the coverage of the ABC array, we are not able to infer whether such localized LVZ is typical for the CHF, or it just occurs in the Binchuan area. Thus, we deployed a ~5 km linear array crossing the northern segment of the CHF and this array was not covered by the ABC array (Fig. 2b). The newly deployed arrays have been in operation in the field from January 5th, 2018 to the end of February 2018.

We inspected the waveforms of stacked airgun signals on the newly deployed linear arrays. As expected, P waves first arrived at stations in the northwest of the southern array, and moved out as the epicentral

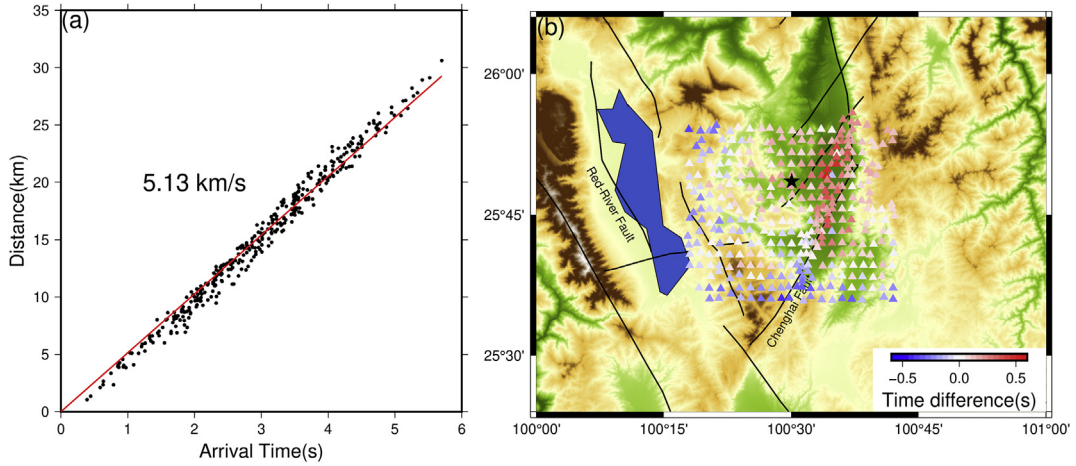

Fig. 4. P-wave travel times of the airgun shot signal. (a) Black dots denote the arrival times at different stations of the ABC array. Red line is the best fit of all travel times whose slope is 5.13 km/s. (b) Differential times between observations and the best-fit arrivals. The black pentagram denotes the airgun location.

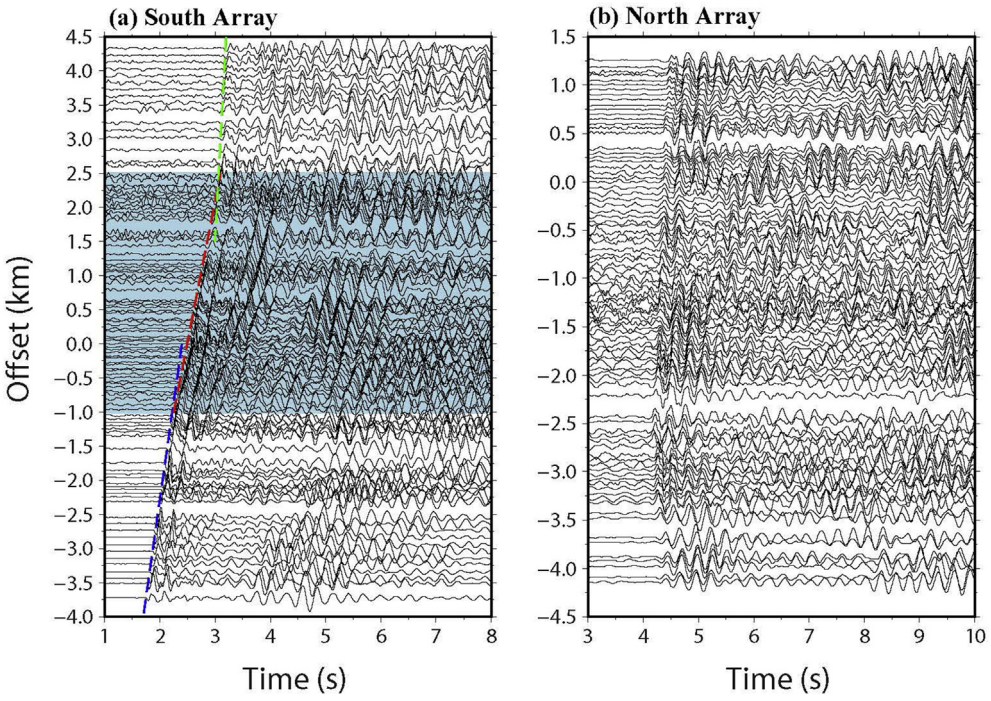

Fig. 5. Cross section of stacked airgun signals recorded at vertical components of the two linear arrays across the Chenghai fault. (a) southern array. Hand-picked first arrivals were indicated by different colors on stations northwest to (blue), within (red), and southeast (green) to the low velocity zone (shadow). (b) northern array.

distances increase (Fig. 5a). The move-out pattern clearly exhibits a change at ~1.0 km in the northwest, with a slower apparent velocity until the station at ~2.5 km in the southeast (Fig. 5a). Then the travel time curve bounced back. Such across-array travel time pattern indicates a LVZ with a width of ~3.5 km, consistent with the results from teleseismic travel times and ambient noise tomography (Yang et al., 2020a). In contrast, the travel times of P waves recorded at the northern array do not show such across-array delay (Fig. 5b), suggesting no obvious LVZ. Thus, the LVZ along the CHF changes significantly in the distance of ~40 km.

5. Discussion

5.1. Short-period dense arrays across faults

Spatially dense arrays have long been used to investigate fine structures of low-velocity fault zones. In early studies of fault zone waves, small-aperture linear arrays had often been deployed across faults to record local earthquakes for a few months (e.g. Li and Vernon, 2001; Li et al., 2002). Sometimes the arrays were deployed in a very short distance so that they may not have captured both boundaries of the LVZ well (Yang and Zhu, 2010), which may also significantly limit the resolution to image the LVZ at greater depths (e.g. Yang et al., 2014). Since the discovery of a 1.5-km wide LVZ along the Calico fault in the eastern California shear zone based on InSAR observations (Fialko et al., 2002), a dense array of 100 seismometers have been installed in a 1.5 km × 5.5 km region across the fault in 2004 (Cochran et al., 2009). High-quality waveforms recorded by this dense array not only allowed better constraints on the LVZ structure from the trapped waves and reflected body waves (Cochran et al., 2009; Yang et al., 2011), but also facilitated the application of newly developed techniques in imaging FZ structure such as the ambient noise cross correlation (ANCC) method (e.g., Zhang and Gerstoft, 2014; Hillers et al., 2014).

More recently, such dense arrays have been deployed across fault zones in southern California with larger aperture and smaller interstation distance, in which fault zone waves with unprecedented quality were recorded (e.g., Schmandt and Clayton, 2013; Ben-Zion et al., 2015). For instance, the waveforms recorded at the 5200-geophone array (120 m of mean spacing between stations) in the Long Beach area showed distinct features of multiple waves reflected from the FZ that had not been previously observed (Yang, 2015). Furthermore, a dense array with a minimal interstation distance of 10 m across the San Jacinto Fault has recorded several striking features. In addition to some FZ trapped waves, the array has also captured numerous spikes and bursts of high-frequency waves that facilitated the detection of a large number of seismic sources, which were not detected by the surrounding permanent network stations (e.g. Meng and Ben-Zion, 2018).

Previously deployed dense arrays for high-resolution imaging of the fault zone structures were mostly composed of a large number of single-component geophones called nodes (e.g., Schmandt and Clayton, 2013; Ben-Zion et al., 2015) or a limited number of three-component short-period instruments (e.g., Li et al., 2007; Yang and Zhu, 2010; Yang et al., 2014). Recently, several studies have started to utilize three-component nodal geophones deployed in 1-D or 2-D settings to detect microearthquakes and image fault zone and crustal structures (e.g., Wang et al., 2019). In addition, the lower frequency limits of such instruments are usually higher than 1 Hz. In our experiment, we used the three-component instruments that have flat response down to 5 s. According to the number of instruments (>600) and aperture, to our best knowledge, the Binchuan multi-scale dense array is the first one using such an unprecedented number of three-component intermediate-band instruments to illuminate fault zone structures.

5.2. Imaging crustal structure from dense arrays

The waveform recordings at the three-component seismometers can also be analyzed by other techniques such as Receiver Functions (RFs). In order to test the reliability of RFs from the intermediate-period instruments, we compared the RFs with that derived from a nearby broadband station (less than 2 km), which has been in operation until December 2015 (Fig. 6b), but was unfortunately removed before the deployment of our dense array. Therefore, the events used to compute

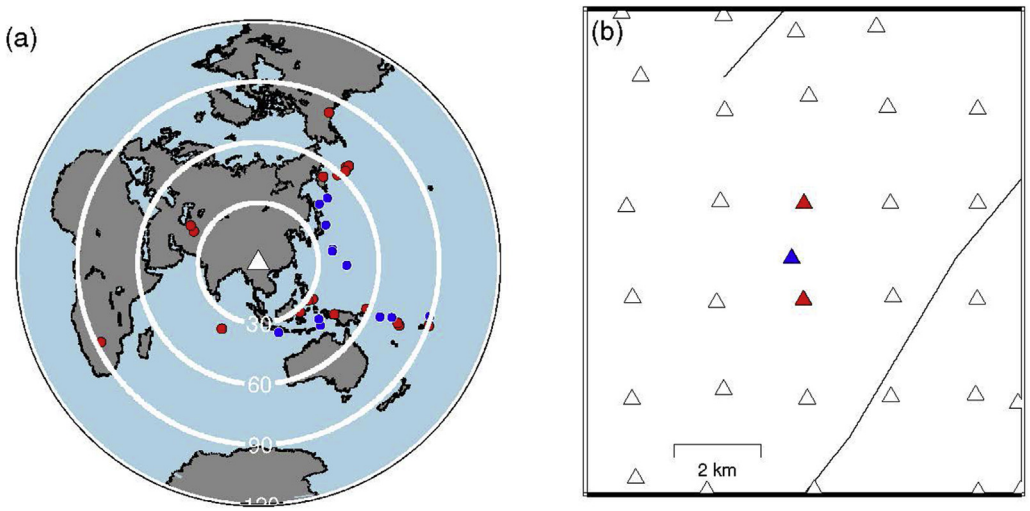

Fig. 6. Distribution of events and stations. The red and blue circles in (a) indicate the events for RFs calculation from intermediate-period and broadband stations, whose locations are shown in (b) by red and blue triangles, respectively.

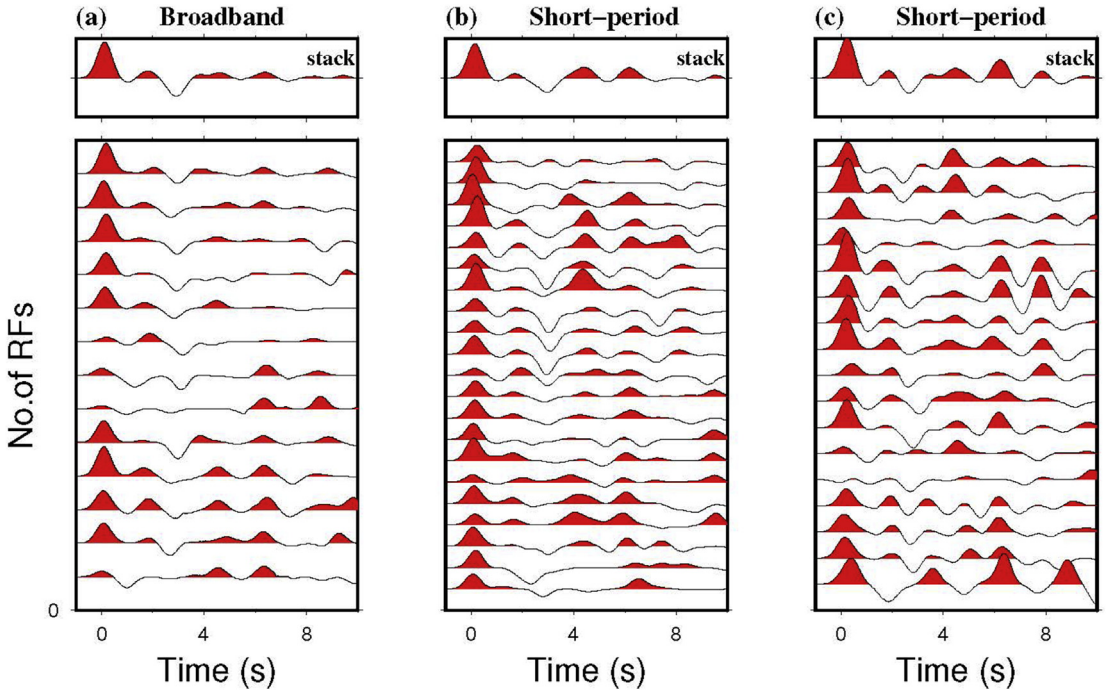

Fig. 7. Comparison of RFs from one broadband station and two nearby intermediate-period seismic stations. (a) RFs record at the broadband station. The RFs are sorted by back azimuth with an equal spacing and the top plot is the stacked waveform of all RFs. (b) and (c) show RFs at the intermediate-period stations.

RFs are different from those on intermediate-period stations (Fig. 6a). We collected 13 teleseismic earthquakes with M_b>5.5 to compute individual and stacked RFs at the broadband station (Fig. 7a). As a result, all RFs show a high signal-to-noise ratio and nearly identical waveforms. The stacked RFs show the Moho phase at ~6.3 s, preceded by a positive phase at ~4.6 s and a negative phase at ~2.9 s. In comparison, RFs from two intermediate-period stations are presented in Fig. 7b and c. Although the teleseismic events are different and each individual RF exhibits slight different features, the stacked RFs indicate nearly identical phases: the Moho phase at ~6.2 s and two others at ~2.9 s and ~4.5 s, respectively. The coherency of the RFs between broadband and intermediate-period stations suggests that it is reliable to derive crustal structures using RFs obtained by the intermediate-period instruments, as they are consistent with other recent studies using nodal geophones (Ward and Lin, 2017).

Indeed, we have computed the RFs on the 2-D ABC array and applied both H-κ and common-conversion-point stacking methods to derive crustal thickness (Jiang et al., 2021a,b). The results show an average crust thickness of 42 km beneath the Binchuan basin and the Moho depth increases from 40 km in the south to 46 km in the north, despite the relatively small array aperture (Jiang et al., 2020; 2021). In addition, we anticipate observing coherent intra-crustal structures such as the depth extent of the LVZ from different approaches such as noise interferometry (She et al., 2019) and dense-array-based receiver functions (Jiang et al., 2021), given the large number of instruments and much smaller inter-station spacing of the newly deployed 1-D across-fault array.

5.3. Temporal changes of fault zones

Compared with the derivation of the LVZ structure, it is more challenging to document temporal changes of fault zones (Yang, 2015). By far most reports on fault zone changes are in post-seismic phases. For example, more than 5 years of ambient noise data have been used to derive the velocity changes over time at the San Andreas Fault near Parkfield. The results illustrated the coseismic damages due to the 2003 M6.5 San Simeon and the 2004 M6.0 Parkfield earthquakes and the subsequent healing process, i.e., increase in velocity (Brenguier et al., 2008). Such healing process in fault zones was also reflected by velocity elevations after major earthquakes, e.g. the 2008 Wenchuan earthquake (Liu et al., 2014), as well as the 1999 M_W 7.6 Izmit and M_W 7.1 Duzce earthquakes (Peng and Ben-Zion, 2006). The healing on the Longmenshan Fault Zone was suggested to accelerate right after the nearby 2013 M_W 6.6 Lushan earthquake (Pei et al., 2019).

However, there is basically no convincing report of temporal changes associated with the preparation process of an earthquake. Indeed, little is known about how earthquakes nucleate, including the size of nucleation zone and where they may initiate. On a heterogeneous fault, the location of the nucleation zone is critical to determine how large an earthquake might become, i.e. different hypocenters lead to different rupture extents and magnitudes because of the finite effective seismogenic zone (Yang et al., 2019a). Furthermore, it has been pointed out that the nucleation location may also determine slip distribution on the ruptured fault (Yao and Yang, 2021). For two neighboring hypocenters, one may develop into a surface breaching rupture with significant shallow slip while the other does not even rupture the ground (Yao and Yang, 2021), despite the identical initial stress distribution and material properties. Acceleration of small-magnitude foreshocks with nearly identical waveforms before the 1999 Izmit Mw 7.6 earthquake has been reported, but it remains in debate whether such intense foreshock sequence reflected a preslip within the nucleation zone of the mainshock (Bouchon et al., 2011) or just a cascading manner of foreshock migration (Ellsworth and Bulut, 2018). Since earthquakes represent rapid fault movement (in a rate of m/s), there are at least 9 folds of magnitude changes in slip rate from tectonic loading (mm-cm/yr) to seismic slip rate. The 9-fold change in fault slip rates will presumably produce appreciable ground deformation, which however remains elusive probably due to low signal-to-noise ratio. One unknown factor is how fast or slow such changes in fault slip rates have occurred. If the acceleration in fault slip rates occur in a short time scale similar to what was reported in laboratory experiments, i.e. seconds (e.g. Zhuo et al., 2018), then it is not practical to derive reliable temporal changes of subsurface. However, a few large to great earthquakes were reported with precursory process lasting for weeks (Kato et al., 2012; Ruiz et al., 2014), increasing the possibility to derive such small temporal changes of subsurface structure from high-quality repeating sources, such as the FASTS.

Compared with the rather unknown time scale of nucleation process of earthquakes, strain accumulation on faults is a long-term process which may last hundreds to thousands of years. Temporal changes of subsurface structure during the interseismic period in Binchuan basin can be readily observed on the FASTS network stations (Luan et al., 2016, 2017; Wang et al., 2020). However, it remains difficult to infer whether such changes are associated with tectonic deformation that accumulates on faults or localized human activities (Luan et al., 2016). More recently, systematic near-surface daily variations have been derived using one month data with frequency airgun shots (1 h per shot) and such changes were best correlated with atmospheric forcing such as temperature variation (Luan et al., 2017). It poses a significant challenge to capture small changes within the fault zone that are caused by deep tectonic loading and thus are expected to reflect different processes associated with earthquakes. Although near-surface changes from non-tectonic sources (e.g. atmospheric forces and human activities) may be inevitable and may control earthquake occurrence in certain circumstances (e.g. Yang et al., 2017; Hsu et al., 2021), we expect to observe different patterns of temporal changes for on- and off-fault stations if the signals from fault movements and their changes rates are above noise level. Therefore, our first multiple-scale dense arrays across fault within a short distance of the FASTS source could provide unprecedented resolution to derive temporal changes of the subsurface fault zone properties at seismogenic depth. However, it is noted that most earthquakes nucleate at depths around 10 km or deeper (Yang and Yao, 2021), despite some outliers which nucleate at shallow depths such as 1 km (Yang et al., 2020b). To infer changes at the seismogenic depth may require stations in further distance, to which the single airgun signal may be obscured within noise. Stacking multiple airgun shots can overcome such a problem, but may reduce the temporal resolution and introduce the source effects of airgun. These problems need to be considered and further explored in future studies.

5.4. Summary

In this work we report the first multiple-scale dense arrays that were deployed to investigate high-resolution fault zone structures in Binchuan, Yunnan, China. In addition to applying different methods to illuminate the CHF features (e.g. fault zone trapped waves and reflected body waves, ANCC, and etc.), we may also derive the temporal changes of the fault and neighboring crust utilizing the high-quality artificial source, although challenges from a variety of aspects have to be overcome, including the influence of atmospheric processes on subsurface changes. The results will not only advance our understanding on the fault zone structures and its evolution over time, but will also facilitate the detection of a large number of small local earthquakes that would be otherwise missed by regular network stations. As evidenced in the recently deployed arrays in southern California, earthquakes at depths extending to lower crust and upper mantle have been discovered in Long Beach, southern California, which significantly advances our understanding of seismogenic behavior for crustal faults (Inbal et al., 2016). The waveforms recorded at our dense array might also facilitate the detection of such deep earthquakes and/or tectonic tremor in the region, thereby advancing our understanding of potential seismic hazards in the region, as well as the deformation pattern in the lower crust due to the India-Eurasia collision. Moreover, the data will allow high-resolution imaging of shallow structures, which is critical for ground motion prediction so as to better prepare for seismic hazards in the region.

Acknowledgement

This work is supported by National Key R&D Program of China (2018YFC1503400), China Earthquake Science Experiment Project, CEA (grants no. 2018CSES0101, 2018CSES0102, 2019CSES0107), HKSAR Research Grant Council GRF Grant 14305617, National Science Foundation of China (grants 41774071, 41974069, 41790463, and 41674058), and Chen Yong Academician Workstation of Yunnan Province in China (2014IC007). The authors thank Dr. Zhigang Peng and two anonymous reviewers for their constructive comments which help improve the paper.

References

Allen, C.R., Gillespie, A.R., Han, Y., Sieh, K.E., Zhang, B., Zhu, C., 1984. Red River and associated faults, Yunnan Province, China: quaternary geology, slip rates, and seismic hazard. Geol. Soc. Am. Bull. 95, 686–700.

Avallone, A., Rovelli, A., Giulio, G.D., Improta, L., Ben-Zion, Y., Milana, G., Cara, F., 2014. Wave-guide effects in very high rate GPS record of the 6 April 2009, M_w 6.1 L'Aquila, central Italy earthquake. J. Geophys. Res. 119. https://doi.org/10.1002/2013JB010475.

Ben-Zion, Y., Sammis, C.G., 2003. Characterization of fault zones. Pure Appl. Geophys. 160, 677–715.

Ben-Zion, Y., Vernon, F.L., Ozakin, Y., Zigone, D., Ross, Z.E., Meng, H., White, M., Reyes, J., Hollis, D., Barklarge, M., 2015. Basic data features and results from a spatially dense seismic array on the San Jacinto fault zone. Geophys. J. Int. https://doi.org/10.1093/gji/ggv142.

Bhat, H.S., Olives, M., Dmowska, R., Rice, J.R., 2007. Role of fault branches in earthquake rupture dynamics. J. Geophys. Res. 112 (B11). https://doi.org/10.1029/2007JB005027.

Bouchon, M., Karabulut, H., Aktar, M., Ozalaybey, S., Schmittbuhl, J., Bouin, M.-P., 2011. Extended nucleation of the 1999 M_w 7.6 Izmit earthquake. Science 331 (6019), 877–880. https://doi.org/10.1126/science.1197341.

Brenguier, F., Campillo, M., Hadziioannou, C., Shapiro, N.M., Nadeau, R.M., Larose, E., 2008. Postseismic relaxation along the san andreas fault at Parkfield from continuous seismological observations. Science 321, 1478–1481. https://doi.org/10.1126/science.1160943.

Chen, X., Yang, H., 2020. Effects of seismogenic width and low-velocity zones on estimating slip-weakening distance from near-fault ground deformation. Geophys. J. Int. https://doi.org/10.1093/gji/ggaa385.

Chen, X., Yang, H., Jin, M., 2021. Inferring critical slip-weakening distance from near-fault accelerogram of the 2014 Mw 6.2 Ludian earthquake. Seismol Res. Lett. https://doi.org/10.1785/0220210089.

Chen, Y., Wang, B., Yao, H., 2017. Seismic airgun exploration of continental crust structures. Sci. China Earth Sci. https://doi.org/10.1007/s11430-016-9096-6.

Chester, F.M., Logan, J.M., 1986. Implications for mechanical properties of brittle faults from observations of the Punchbowl Fault zone, California. Pure Appl. Geophys. 124, 79–106.

Chester, F.M., Evans, J.P., Biegel, R.L., 1993. Internal structure and weakening mechanisms of the San Andreas fault. J. Geophys. Res. 98, 771–786.

Cochran, E.S., Li, Y., Shearer, P.M., Barbot, S., Fialko, Y., Vidale, J.E., 2009. Seismic and geodetic evidence for extensive, long-lived fault damage zones. Geology 37, 315–318. https://doi.org/10.1130/G25306A.1.

Duan, B., Oglesby, D.D., 2006. Heterogeneous fault stresses from previous earthquakes and the effect on dynamics of parallel strike-slip faults. J. Geophys. Res. 111 (B5). https://doi.org/10.1029/2005JB004138.

Eberhart-Phillips, D., Stanley, W.D., Rodriguez, B.D., Lutter, W.J., 1995. Surface seismic and electrical methods to detect fluids related to faulting. J. Geophys. Res. 97, 12,919–12,936.

Ellsworth, W.L., Bulut, F., 2018. Nucleation of the 1999 Izmit earthquake by a triggered cascade of foreshocks. Nat. Geosci. 11, 531–535.

Faulkner, D.R., Mitchell, T.M., Healy, D., Heap, M.J., 2006. Slip on 'weak' faults by the rotation of regional stress in the fracture damage zone. Nature 444. https://doi.org/10.1038/nature05353.

Faulkner, D.R., Jackson, C.A.L., Lunn, R.J., Schlische, R.W., Shipton, Z.K., Wibberley, C.A.J., Withjack, M.O., 2010. A review of recent developments concerning the structure, mechanics and fluid flow properties of fault zones. J. Struct. Geol. 32, 1557–1575. https://doi.org/10.1016/j.jsg.2010.06.009.

Fialko, Y., Sandwell, D., Agnew, D., Simons, M., Shearer, P., Minster, B., 2002. Deformation on nearby faults induced by the 1999 Hector Mine earthquake. Science 297, 1858–1862. https://doi.org/10.1126/science.1074671.

Finzi, Y., Hearn, E.H., Ben-Zion, Y., Lyakhovsky, V., 2009. Structural properties and deformation patterns of evolving strike-slip faults: numerical simulations incorporating damage rheology. Pure Appl. Geophys. 166, 1537–1573. https://doi.org/10.1007/s00024-009-0522-1.

Harris, R.A., Day, S.M., 1997. Effects of a low-velocity zone on a dynamic rupture. Bull. Seismol. Soc. Am. 87, 1267–1280.

Hillers, G., Campillo, M., Ben-Zion, Y., Roux, P., 2014. Seismic fault zone trapped noise. J. Geophys. Res. 119. https://doi.org/10.1002/2014JB011217.

Hsu, Y., Kao, H., Burgmann, R., Lee, Y., Huang, H., Hsu, Y., Wu, Y., Zhuang, J., 2021. Synchronized and asynchronous modulation of seismicity by hydrological loading: a case study in Taiwan. Sci. Advances 7 (16). https://doi.org/10.1126/sciadv.abf7282.

Huang, Y., Ampuero, J.P., 2011. Pulse-like ruptures induced by low-velocity fault zones. J. Geophys. Res. 116.

Huang, Y., Ampuero, J.P., Helmberger, D.V., 2014. Earthquake ruptures modulated by waves in damaged fault zones. J. Geophys. Res. 119, 3133–3154.

Inbal, A., Ampuero, J.P., Clayton, R.W., 2016. Localized seismic deformation in the upper mantle revealed by dense seismic arrays. Science. https://doi.org/10.1126/science.aaf1370.

Jiang, X., Yang, H., Yang, W., Wang, W., 2020. Crustal structure in the Binchuan Basin of Yunnan constrained from receiver functions on a 2-D seismic dense array. Earthquake Science 33, 264–272. https://doi.org/10.29382/eqs-2020-0264-01.

Jiang, X., Hu, S., Yang, H., 2021. Depth extent and Vp/Vs ratio of the Chenghai fault zone, Yunnan, China constrained from dense-array-based teleseismic receiver functions. J. Geophys. Res. https://doi.org/10.1029/2021JB022190.

Johnson, A.M., Fleming, R.W., Cruikshank, K.M., 1994. Shear zones formed along long, straight traces of fault zones during the 28 June 1992 Landers, California earthquake. Bull. Seismol. Soc. Am. 84, 499–510.

Kanamori, H., 1994. Mechanics of earthquakes. Annu. Rev. Earth Planet Sci. 22, 207–237.

Kaneko, Y., Ampuero, J.P., Lapusta, N., 2011. Spectral-element simulations of long-term fault slip: effect of low-rigidity layers on earthquake-cycle dynamics. J. Geophys. Res. 116 (B10313). https://doi.org/10.1029/2011JB008395.

Kato, A., Obara, K., Igarashi, T., Tsuruoka, H., Nakagawa, S., Hirata, N., 2012. Propagation of slow slip leading up to the 2011 Mw 9.0 Tohoku-Oki earthquake. Science 335 (6069), 705–708. https://doi.org/10.1126/science.1215141.

Li, H., Zhu, L., Yang, H., 2007. High-resolution structures of the Landers fault zone inferred from aftershock waveform data. Geophys. J. Int. 171, 1295–1307. https://doi.org/10.1111/j.1365-246X.2007.03608.x.

Li, Y., Vidale, J.E., Aki, K., Xu, F., Burdette, T., 1998. Evidence of shallow fault zone strengthening after the 1992 *M* 7.5 Landers, California, earthquake. Science 279, 217–219.

Li, Y., Vidale, J.E., Day, S.M., Oglesby, D.D., the SCEC Field Working Team, 2002. Study of the 1999 M 7.1 Hector Mine, California, earthquake fault plane by trapped waves. Bull. Seismol. Soc. Am. 92, 1318–1332.

Li, Y., Vernon, F.L., 2001. Characterization of the San Jacinto fault zone near Anza, California, by fault zone trapped waves. J. Geophys. Res. 106, 30,671–30,688.

Liu, C., Yang, H., Wang, B., Yang, J., 2021. Impacts of reservoir water level fluctuation on measuring seasonal seismic travel time changes in the Binchuan basin, Yunnan, China. Rem. Sens. 13,, 2421, https://doi.org/10.3390/rs13122421.

Liu, Z., Huang, J., Peng, Z., Su, J., 2014. Seismic velocity changes in the epicentral region of the 2008 Wenchuan earthquake measured from three-component ambient noise correlation techniques. Geophys. Res. Lett. 41 (1), 37–42. https://doi.org/10.1002/2013GL058682.

Luan, Y., Yang, H., Wang, B., 2016. Large volume air-gun waveform data processing (I): Binchuan, Yunnan. Earthq. Res. China 32 (2), 305–318.

Luan, Yi, Yang, H., Wang, B., 2017. Seasonal and daily variations of subsurface velocity revealed by the air-gun source in binchuan, yunnan, China. In: AGU Fall Meeting Abstract: S33A-0847, 2017, New Orleans, USA.

Ma, K., et al., 2006. Slip zone and energetics of a large earthquake from the taiwan chelungpu-fault drilling Project. Nature 444, 473–476.

Meng, H., Ben-Zion, Y., 2018. Detection of small earthquakes with dense array data: example from the San Jacinto fault zone, southern California. GJI 212, 442–457. https://doi.org/10.1093/gji/ggx404.

Pei, S., Niu, F., Ben-Zion, Y., Sun, Q., Liu, Y., Xue, X., Ru, J., Shao, Z., 2019. Seismic velocity reduction and accelerated recovery due to earthquakes on the Longmenshan fault. Nat. Geosci. 12, 387–392. https://doi.org/10.1038/s41561-019-0347-1.

Peng, Z., Ben-Zion, Y., 2006. Temporal changes of shallow seismic velocity around the Karadere-Duzce branch of the North Anatolian fault and strong ground motion. Pure Appl. Geophys. 163, 567–599.

Ripperger, J., Ampuero, J.-P., Mai, P.M., Giardini, D., 2007. Earthquake source characteristics from dynamic rupture with constrained stochastic fault stress. J. Geophys. Res. 112 (B4). https://doi.org/10.1029/2006JB004515.

Rubinstein, J.L., Beroza, G.C., 2004. Evidence for widespread nonlinear strong ground motion in the Mw 6.9 Loma Prieta earthquake. Bull. Seismol. Soc. Am. 94, 1595–1608.

Ruiz, S., Metois, M., Fuenzalida, A., Ruiz, J., Leyton, F., Grandin, R., Vigny, C., Madariaga, R., Campos, J., 2014. Intense foreshocks and a slow slip event preceded the 2014 Iquique M_w 8.1 earthquake. Science 345 (6201), 1165–1169. https://doi.org/10.1126/science.1256074.

Ryan, K.J., Oglesby, D.D., 2014. Dynamically modelling fault step overs using various friction laws. J. Geophys. Res. 119 (7). https://doi.org/10.1002/2014JB011151.

Schaff, D.P., Beroza, G.C., 2004. Coseismic and postseismic velocity changes measured by repeating earthquakes. J. Geophys. Res. 109, B10302. https://doi.org/10.1029/2004JB003011.

Schmandt, B., Clayton, R.W., 2013. Analysis of teleseismic P waves with a 5200-station array in long Beach, California: evidence for an abrupt boundary to inner borderland rifting. J. Geophys. Res. 118, 5320–5338. https://doi.org/10.1002/jgrb.50370.

Schulz, S.E., Evans, J.P., 1998. Spatial variability in microscopic deformation and composition of the Punchbowl fault, southern California: implications for mechanisms, fluid-rock interaction, and fault morphology. Tectonophysics 295, 223–244.

Schulz, S.E., Evans, J.P., 2000. Mesoscopic structure of the Punchbowl Fault, Southern California and the geologic and geophysical structure of active strike-slip faults. J. Struct. Geol. 22, 913–930.

She, Y., Yao, H., Yang, H., Feng, J., 2019. Retrieval of the P wave reflections across the Chenghai fault zone from the autocorrelation and cross-correlation of ambient seismic noise. In: AGU Fall Meeting Abstract No.S23C-0643.

Sieh, K., et al., 1993. Near-field investigations of the Landers earthquake sequence, april to July 1992. Science 260, 171–176.

Song, J., Yang, H., 2021. Seismic site response inferred from records at a dense linear array across the Chenghai fault zone. Binchuan, Yunnan, J. Geophys. Res., in revision.

Ujiie, K., et al., 2013. Low coseismic shear stress on the Tohoku-Oki megathrust determined from laboratory experiments. Science 342, 1211–1214.

Vidale, J.E., Li, Y., 2003. Damage to the shallow Landers fault from the nearby Hector Mine earthquake. Nature 421, 524–526.

Wang, B., Wu, G., Su, Y., Wang, B., Ge, H., Jin, M., Yang, J., Zhang, Q., Li, T., Liu, J., 2015. Site construction of the Binchuan transmitting seismic stations and preliminary observational data. J. Seismol. Res. 38 (1), 1–6.

Wang, B., Ge, H., Yang, W., Wang, W., Wang, B., Wu, G., Su, Y., 2012. Transmitting seismic station monitors fault zone at depth. Eos Trans. AGU 93 (5), 49–50.

Wang, B., Yang, W., Wang, W., Yang, J., Li, X., Ye, B., 2020. Diurnal and semidiurnal P- and S-wave velocity changes measured using an airgun source. J. Geophys. Res. https://doi.org/10.1029/2019JB018218.

Wang, Y., Lin, F.-C., Ward, K.M., 2019. Ambient noise tomography across the Cascadia subduction zone using dense linear seismic arrays and double beamforming. Geophys. J. Int. 217 (3), 1668–1680. https://doi.org/10.1093/gji/ggz109.

Ward, K.M., Lin, F.-C., 2017. On the viability of using autonomous three-component nodal geophones to calculate teleseismic ps receiver functions with an application to old faithful, yellowstone. Seismol Res. Lett. https://doi.org/10.1785/0220170051.

Weng, H., Huang, J., Yang, H., 2015. Barrier-induced supershear ruptures on a slip-weakening fault. Geophys. Res. Lett. 42 (12), 4824–4832.

Weng, H., Yang, H., Zhang, Z., Chen, X., 2016. Earthquake rupture extents and coseismic slips promoted by damaged fault zones. J. Geophys. Res. 121 (6), 4445–4457. https://doi.org/10.1002/2015JB012713.

Weng, H., Yang, H., 2018. Constraining frictional properties on fault by dynamic rupture simulations and near-field observations. J. Geophys. Res. 123, 6658–6670. https://doi.org/10.1029/2017JB015414 https://doi.org/10.1029/2017JB015414.

Wibberley, C.A.J., Yielding, G., Toro, G.D., 2008. Recent advances in the understanding of fault zone internal structure: a review. In: Structure of Fault Zones: Implications for Mechanical and Fluid-Flow Properties, vol. 299. Geological Society of London Special Publication, pp. 5–33. https://doi.org/10.1144/SP299.2.

Wu, C., Peng, Z., Ben-Zion, Y., 2009. Non-linearity and temporal changes of fault zone site response associated with strong ground motion. Geophys. J. Int. 176, 265–278. https://doi.org/10.1111/j.1365-246X.2008.04005.x.

Xu, Y., Wang, B., Wang, W., Zhang, B., Sun, T., 2018. Multiple seismological evidences of basin effects revealed by Array of Binchuan (ABC), northwest Yunnan, China. Earthq. Sci. 31, 281–290. https://doi.org/10.29382/eqs-2018-0281-8.

Xu, Y., Koper, K.D., Burlacu, R., Herrmann, R.B., Li, D., 2020. A new uniform moment tensor catalog for Yunnan, China, from January 2000 through December 2014, *Seismo*. Res. Lett. 91, 891–900. https://doi.org/10.1785/0220190242.

Yang, H., 2015. Recent advances in imaging crustal fault zones: a review. Earthq. Sci. 28 (2), 151–162. https://doi.org/10.1007/s11589-015-0114-3.

Yang, H., Li, Z., Peng, Z., Ben-Zion, Y., Vernon, F., 2014. Low velocity zones along the San Jacinto Fault, Southern California, from body waves recorded in dense linear arrays. J. Geophys. Res. https://doi.org/10.1002/2014JB011548.

Yang, H., Liu, Y., Wei, M., Zhuang, J., Zhou, S., 2017. Induced earthquakes in the development of unconventional energy resources. Sci. China Earth Sci. 60 (9), 1632–1644. https://doi.org/10.1007/s11430-017-9063-0.

Yang, H., Zhu, L., 2010. Shallow low-velocity zone of the San Jacinto fault from local earthquake waveform modeling. Geophys. J. Int. 183 (1), 421–432. https://doi.org/10.1111/j.1365-246X.2010.04744.x.

Yang, H., Yao, S., 2021. Shallow destructive earthquakes. Earthq. Sci. 34 (1). https://doi.org/10.29382/eqs-2020-0072.

Yang, H., Zhu, L., Cochran, E.S., 2011. Seismic structures of the Calico fault zone inferred from local earthquake travel time modelling. Geophys. J. Int. 186, 760–770.

Yang, H., Liu, Y., Lin, J., 2012. Effects of subducted seamount on megathrust earthquake nucleation and rupture propagation. Geophys. Res. Lett. 39, L24302.

Yang, H., Liu, Y., Lin, J., 2013. Geometrical effects of a subducted seamount on stopping megathrust ruptures. Geophys. Res. Lett. 40, 2011–2016.

Yang, H., Yao, S., He, B., Newman, A.V., 2019a. Earthquake rupture dependence on hypocentral location along the Nicoya Peninsula subduction megathrust. Earth Planet Sci. Lett. 520, 10–17.

Yang, H., Yao, S., He, B., Newman, A.V., Weng, H., 2019b. Deriving rupture scenarios from interseismic locking distributions along the subduction megathrust. J. Geophys. Res. 124 (10), 10376–10392. https://doi.org/10.1029/2019JB017541.

Yang, H., Duan, Y., Song, J., Jiang, X., Tian, X., Yang, W., Wang, W., Yang, J., 2020a. Fine structure of the Chenghai fault zone, Yunnan, China constrained from teleseismic travel time and ambient noise tomography. J. Geophys. Res. 125, 7. https://doi.org/10.1029/2020JB019565.

Yang, H., Zhou, P., Fang, N., Zhu, G., Xu, W., Su, J., Meng, F., Chu, R., 2020b. A shallow shock: the 25 February 2019 M_L 4.9 earthquake in the Weiyuan shale gas field in Sichuan, China. Seismol Res. Lett. https://doi.org/10.1785/0220200202.

Yang, W., Wang, B., Yuan, S., Ge, H., 2018. Temporal variation of seismic-wave velocity associated with groundwater level observed by a downhole airgun near the Xiaojiang Fault Zone. Seismol Res. Lett. 89 (3), 1014–1022. https://doi.org/10.1785/0220170282.

Yao, S., Yang, H., 2020. Rupture dynamics of the 2012 nicoya Mw 7.6 earthquake: evidence for low strength on the megathrust. Geophys. Res. Lett. 47. https://doi.org/10.1029/2020GL087508 e2020GL087508.

Yao, S., Yang, H., 2021. Hypocentral dependent shallow slip distribution and rupture extents along a strike-slip fault, Earth Planet. Sci. Lett. in revision.

Yehya, A., Yang, Z., Rice, J.R., 2018. Effect of fault architecture and permeability evolution on response to fluid injection. J. Geophys. Res. 123 (11). https://doi.org/10.1029/2018JB016550.

Yu, W., Zhang, J., Zhou, G., Wang, J., Zeng, X., 2005. Surface rupture of the 2001 Yongsheng M6 earthquake and Chenghai Fault. J. Seismol. Res. 28 (2), 125–128.

Yu, H., Liu, Y., Yang, H., Ning, J., 2018. Modeling earthquake sequences along the Manila subduction zone: effects of three-dimensional fault geometry. Tectonophysics 733, 73–84. https://doi.org/10.1016/j.tecto.2018.01.025.

Zhang, Y., Liu, J., 2016. Study on characteristics of fault activity and relation between fault activity and earthquakes in Yunnan region. J. Geodesy Geodyn. 36 (6). https://doi.org/10.14075/j.jgg.2016.06.004.

Zhou, Q., Guo, S., Xiang, H., 2004. Principle and method of delineation of potential seismic sources in northeastern Yunnan province. Seismol. Geol. 26 (4), 761–771.

Zhang, Y., Wang, B., Lin, G., Wang, W., Yang, W., Wu, Z., 2020. Upper crustal Vp and vs velocity structures of Binchuan, Yunnan revealed by dense array local seismic tomography. Chin. J. Geophys. 9, 3292–3306.

Zhang, J., Gerstoft, P., 2014. Local-scale cross-correlation of seismic noise from the Calico fault experiment. Earthq. Sci. 27 (3), 311–318. https://doi.org/10.1007/s11589-014-0074-z.

Zhao, P., Peng, Z., 2009. Depth extent of damage zones around the central Calaveras fault from waveform analysis of repeating earthquakes. Geophys. J. Int. https://doi.org/10.1111/j.1365-246X.2009.04385.x.

Zhuo, Y.-Q., Liu, P., Chen, S., Guo, Y., Ma, J., 2018. Laboratory observations of tremor-like events generated during preslip. Geophys. Res. Lett. 45, 6926–6934. https://doi.org/10.1029/2018GL079201.